Journal of Manufacturing Processes 35 (2018) 492–499

Contents lists available at ScienceDirect

Journal of Manufacturing Processes

journal homepage: www.elsevier.com/locate/manpro

Pulsed SLM-manufactured AlSi10Mg alloy: Mechanical properties and microstructural effects of designed laser energy densities

Lin-zhi Wang[a,*,1], Sen Wang[a,1], Xingfu Hong[b]

[a] Chongqing Key Laboratory of Additive Manufacturing Technology and Systems, Chongqing Institute of Green and Intelligent Technology, Chinese Academy of Sciences, Chongqing 400714, PR China

[b] China Aerodynamics Research and Development Center, Mianyang 621000, PR China

ARTICLE INFO

Keywords:
Laser energy density
Microstructure
Mechanical properties
Pulsed selective laser melting
AlSi10Mg

ABSTRACT

The effects of laser energy densities on microstructures and mechanical properties of AlSi10Mg samples fabricated by pulsed selective laser melting (P-SLM) were studied. Scanning electron microscope, transmission electron microscope, X-ray diffraction, Vickers hardness tester and electronic testing machine were used for analysis and measurement of microstructures, phases and mechanical properties of the samples, respectively. The results show that fine cellular microstructures are composed of α-Al, eutectic Si, and secondary Si. Moreover, the microhardness values of the specimens perpendicular to the building directions fluctuate between $HV_{0.1}110 \sim HV_{0.1}130$ while those of the specimens along the building directions decrease with increasing building heights. Finally, comparison of the mechanical properties of P-SLM and casting samples were discussed, the better mechanical properties of P-SLM samples were showed than those of the casting samples, which can be attributed to solid solution strengthening, grain refinement strengthening, dislocations strengthening and second-phase strengthening.

1. Introduction

Aluminum alloys have been ideal lightweight materials because of their excellent specific strength and stiffness, high thermal and electrical conductivity, and fine formability [1]. Hypoeutectic AlSi10Mg is increasingly employed in automotive, aerospace, and aircraft applications for its excellent casting properties, good mechanical properties and corrosion resistance [2,3]. At present, engineering parts made in AlSi10Mg have been fabricated by traditional manufacturing processes such as casting, forging, extrusion, and powder metallurgy. However, some AlSi10Mg alloy parts are normally in complex and irregular configurations, which are difficult to fabricate using the conventional processing methods. Furthermore, the low solidification rates associated with these processes may result in coarsened microstructures with the attendant poor mechanical properties and the large degrees of segregation [4]. Therefore, new processing methods are highly demanded to satisfy the need for obtaining complex components with fine and uniform microstructures.

Additive manufacturing (AM), also known as 3D printing, is a revolutionary digital and green intelligent manufacturing technology based on the design of 3D CAD model and cumulative layered deposition [5,6,7]. A type of AM fabrication known as selective laser melting (SLM) exhibits an exciting potential application in direct fabricating three-dimensional parts with complex structures [8]. Moreover, parts fabricated by SLM can also obtain very fine microstructures with the attendant high strength and hardness due to the rapid solidification rate (up to 10^{6-8} K/s) [9,10]. Kempen et al. [11] researched mechanical properties of AlSi10Mg produced by SLM. They found that SLM AlSi10Mg parts have mechanical properties higher or at least comparable to the casted AlSi10Mg material, because of the very fine microstructure and fine distribution of the Si phase. Brandl et al. [12] researched microstructure of AlSi10Mg samples manufactured by SLM, and found the microstructure was characterized by cellular dendrites of α-Al and interdentritic Si particles. Thijs et al. [13] investigated fine-structured aluminum products with controllable texture by selective laser melting of pre-alloyed AlSi10Mg powder. They observed that the high thermal gradients occurring during SLM lead to a very fine microstructure with submicron-sized cells and a high hardness. Furthermore, a morphological and crystallographic texture is present in the SLM parts. Read et al. [14] studied process optimization and mechanical properties of AlSi10Mg alloy using SLM, they concluded that samples showed better strength and elongation properties, compared to

* Corresponding author.
E-mail address: wlz@cigit.ac.cn (L.-z. Wang).
[1] The contributions of these authors are equivalent.

https://doi.org/10.1016/j.jmapro.2018.09.007
Received 12 November 2017; Accepted 3 September 2018
1526-6125/ © 2018 Published by Elsevier Ltd on behalf of The Society of Manufacturing Engineers.

Table 1
Chemical composition of AlSi10Mg powders.

Element	Cu	Mg	Fe	Si	Mn	Zn	other	Al
Composition (wt %)	0.06	0.623	0.08	9.628	0.01	0.03	< 0.2	Balance

die cast Al-alloys of similar composition.

Above investigations reported the characteristics of microstructures and mechanical properties of AlSi10Mg samples fabricated by a continuous-wave SLM equipment under different process parameters. In this study, a new pulsed SLM (P-SLM) process is proposed. Moreover, microstructure evolutions and mechanical properties of AlSi10Mg using P-SLM by designed laser energy densities are presented. The strengthening mechanisms of mechanical properties are also discussed.

2. Experimental methods and materials

2.1. Powder properties and P-SLM process

The AlSi10Mg powder used in current investigation was argon gas atomized and the powder chemical composition is listed in Table 1.

The P-SLM experiments are carried out by a powder-bed manufacturing machine (provided by Chongqing Institute of Green and Intelligent Technology, Chinese Academy of Sciences). This machine can handle reactive materials in a good controlled argon atmosphere. It is equipped with a 400 W fiber laser and has a laser beam diameter of about 118 μm A meander scan strategy (raster with 67° rotation for each layer) and an aluminum substrate was used for all tests, and the platform temperature was maintained at 160 °C during the whole P-SLM process to reduce residual stresses and distortion of the components. Exposure time and point distance are in the range of 100 ~ 180 μs, and 80 ~ 180 μm respectively.

The laser energy density (LED) describes the effective energy input per volume during P-SLM [15,16]:

$$LED = P/(vhd) \tag{1}$$

where P (W) denotes the laser power, v (mm/s) the scanning velocity, h (mm) the distance between the individual hatch vectors and d (mm) the slice thickness of the individual layers. The LED represents the energy absorbed by unit volume of powders. Further, the scanning velocity v is determined by:

$$v = Pd/Te \tag{2}$$

where Pd (μm) is the point distance and Te (μs) is the exposure time. Therefore, a formula can be drawn that:

$$LED = PTe/(Pdhd) \tag{3}$$

In this study, P = 400 W, h = 0.13 mm, d = 0.025 mm. Consequently,

$$LED = 8 \times 10^5 Te/(7Pd) \tag{4}$$

The LEDs in the SLM process are calculated according to Eq. (4), and typical LED of 89, 109, 131, 174 and 200 J/mm^3 were selected and analyzed in the experiment.

2.2. Microstructure and fracture surface analyses

The cubic sample with dimensions of 10 mm × 10 mm × 10 mm was manufactured. Cross-sections of the specimens were prepared by standard metallographic procedures, including wire cutting, grinding, polishing and etching (vol. 1%HF + vol. 1.5%HCL + vol. 2.5%HNO_3 + vol. 95%H_2O). Microstructure micrographs and fracture surfaces of the SLM processed specimens were obtained using an optical microscopy (Zeiss, Axio Scope.A1) and a field emission scanning electron microscope (JEOL, JSM-7800 F). Energy dispersive X-ray spectroscopy (Oxford, Inc., ISIS300 EDS) was used to detect the elemental distributions and help to determine the phases formed in the SLMed samples. A field emission transmission electron microscope (Tecnai, G2 F30) was used to characterize diffraction patterns. X-ray diffraction (XRD) (using Cu Ka, Panalytical Xpert Pro diffractometer) was used to identify the phases formed in the samples.

2.3. Mechanical properties testing

The Micro-Vickers hardness tests were performed by a Vickers hardness tester (MTH4 microhardness-tester) with a period of 20 s, a load of 100 g and a step size of 0.5 mm. At least twenty measurements were made at X, Y and 45° direction, respectively. Tensile tests were carried out with an electronic testing machine (SANS XYA105C) at room temperature with measuring length of 66 mm, according to EN 10002-1. The vertically and horizontally built samples were tested along their axis and the tensile velocity was 0.5 mm/min. Three tensile test results were collected for every type of specimen and the average values were adopted as results. The dimensions for the tensile specimens were made in two build direction, as illustrated in Fig. 1.

3. Results

3.1. Microstructures

Typical microstructures of the AlSi10Mg parts perpendicular to building directions produced by P-SLM are shown in Fig. 2. The interlayer microstructure features (as seen in Fig. 2(a)) created by the pulsed laser beam has distinguished difference with the elongated teardrop shape molten pool microstructures caused by continuous-wave laser beam movement reported in previous literature [17], the obvious layered structure can be observed, and the elliptical molten pools overlapping each other toward the direction of laser movement. The pulse laser has tens of millisecond gaps between each pulse due to its

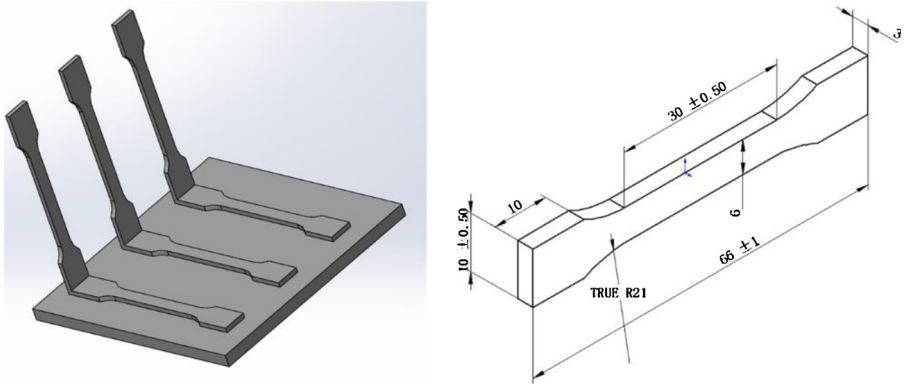

Fig. 1. Diagram of the vertically and horizontally built samples and dimensions for the tensile specimens.

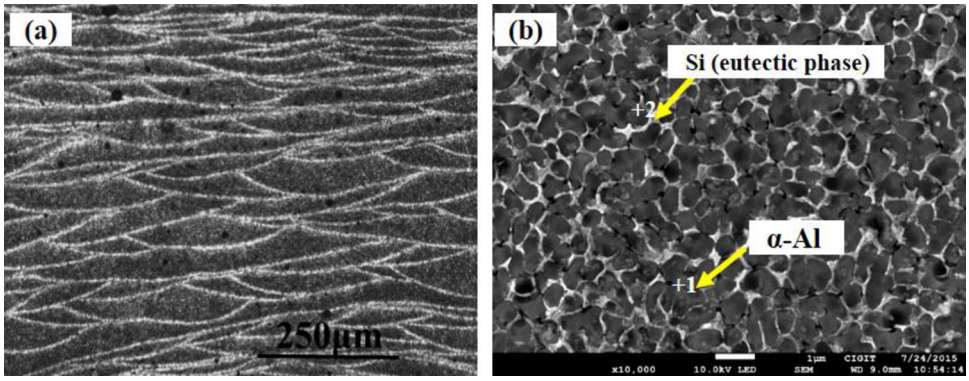

Fig. 2. Typical microstructures of the AlSi10Mg specimens perpendicular to building directions produced by P-SLM: (a) OM image showing interlayer microstructures on cross-sections and (b) The top view microstructure of the top layer.

feature of on/off periods, therefore, each individual molten pool to solidifies before the next laser pulse is fired.

Microstructures including obvious Al matrix and cell boundaries can be observed perpendicular to building directions and the average cell size is approximately 1 μm (as seen in Fig. 2(b)). According to binary phase diagram of Al-Si, gray cellular structure is Al matrix, and white fibrous structure is eutectic Si. Micrographs of this structure can be readily found throughout the literature [18]. Cell size is determined by nucleation rate (N) and growth rate (G), the larger the value of N/G, the easier the formation of fine cells. In the solidification process of AlSi10Mg produced by P-SLM, both the N and G are increased due to extremely fast undercooling caused by fast cooling rate of the liquid metal. However, the N is far greater than the G and then the value of N/G is large. Therefore, cell size of the AlSi10Mg parts fabricated by P-SLM is very fine.

Typical microstructures of the AlSi10Mg parts along the building directions produced by P-SLM are shown in Fig. 3. The microstructures are mainly composed of coarse cellular zone and fine cellular zone. Interlayer bonding is the coarse cellular zone with width of 10 ~ 15 μm. This is because partial re-melting of previously deposited layer (layer n) occurs when processing the fresh layer (layer n + 1). In this case, area adjacent to the fusion line is overheated caused by the thermal effect, and then resulting in the formation of coarse cellular zone. Microstructure of interlayer away from the fusion line is mainly fine cellular zone. This is because the time interval of laser scanning in the same layer is relatively short, and the temperature gradient between the same layers is extremely small. Therefore, it is difficult to form new crystal nuclei quickly. In this case, the growth direction of cell is parallel to the direction of local heat conduction, thus forming the fine cellular crystals.

To analyze further, TEM analysis is done to confirm which type these precipitated phases are in different zones. Fig. 4 shows TEM micrographs of microstructures of the AlSi10Mg sample along the building directions produced by P-SLM. One can see obvious Al matrix and cell

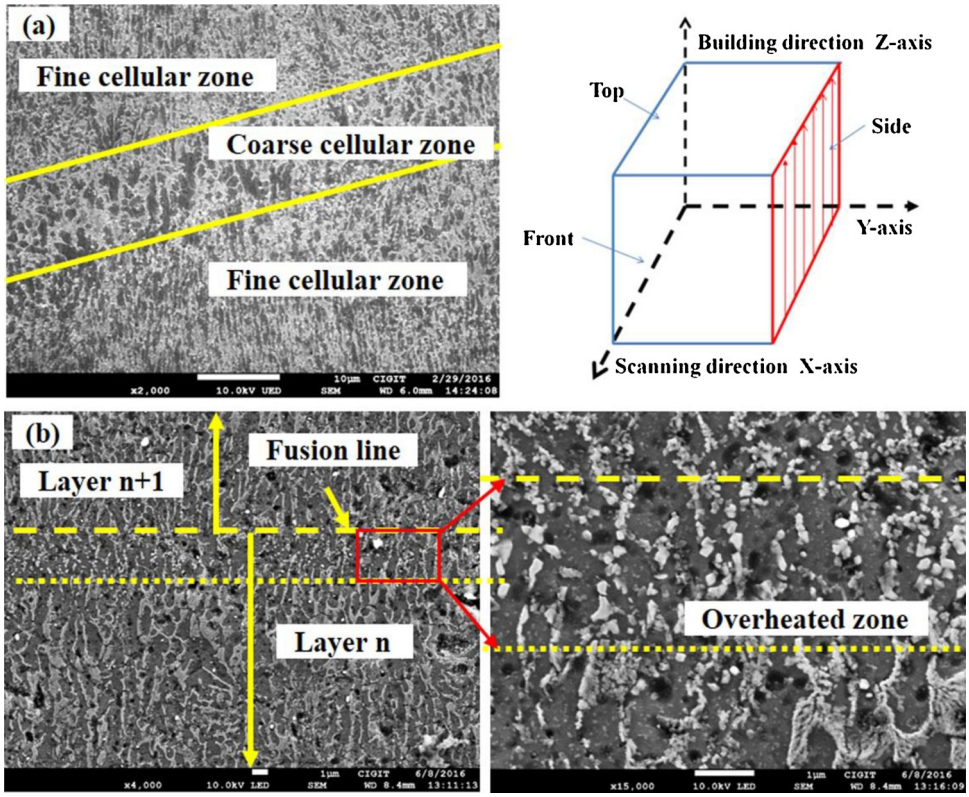

Fig. 3. Typical microstructures of the AlSi10Mg specimens along the building directions produced by P-SLM: (a) Typical microstructure and (b) high resolution image of the microstructure in (a).

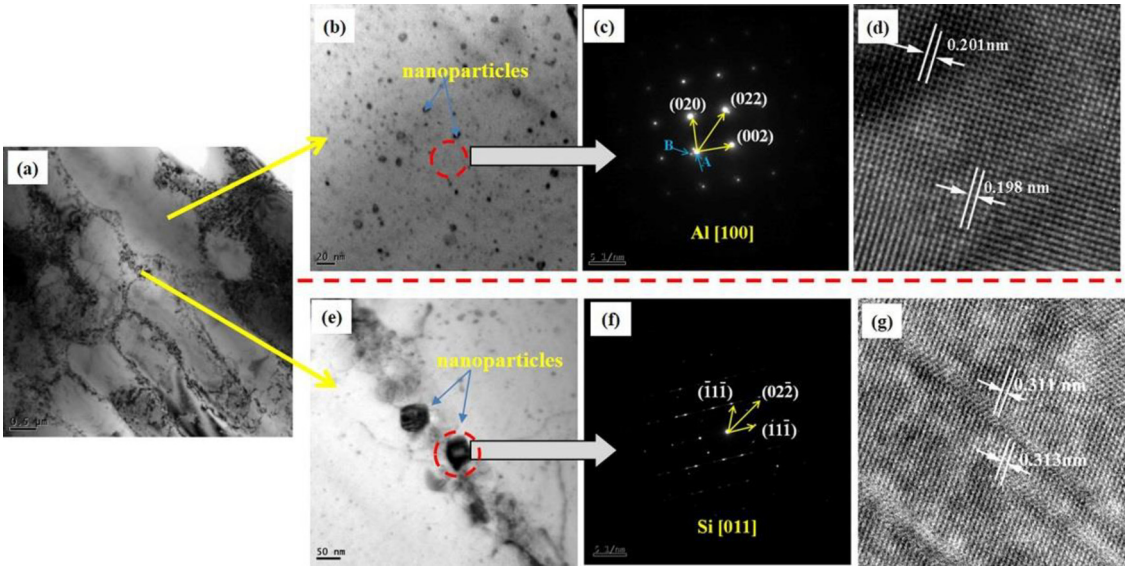

Fig. 4. TEM images of microstructures of the AlSi10Mg sample along the building directions produced by P-SLM: (a) microstructure characteristics; (b) microstructure of matrix; (c) corresponding selected matrix diffraction pattern in (a); (d) high resolution image of the matrix in (a); (e) microstructure of cell boundary; (f) corresponding selected nanoparticle diffraction pattern in (e) and (g) high resolution image of the nanoparticle in (e).

boundary with elongated cellular structure (as seen in Fig. 4(a)). Some nano-scale particles (size of about 5 nm) are distributed uniformly in the Al matrix in Fig. 4(b). The provided selected matrix diffraction pattern (Fig. 4(c)) corresponding to Fig. 4(b) clearly indicates the spot patterns of α-Al with a face-centered cubic structure as well as the periodically arranged two-dimensional diffraction spots of the (020), (022) and (002) planes of Al. Moreover, there are obvious satellite spots in the diffraction pattern (as shown in Fig. 4(c)), which may be produced by double diffractions. In addition, high resolution image of the Al matrix (as shown in Fig. 4(d)) can clearly see lattice fringes, and the lattice spacing is about 0.201 nm, corresponding to the (002) plane of Al, which reveals that those Al matrixes had crystal face preferred orientations.

Larger nanoparticles (size of about 50 nm) are precipitated at the cell boundaries of the Al matrix (as seen in Fig. 4(e)). The provided selected nanoparticle diffraction pattern (Fig. 4(f)) corresponding to Fig. 4(e) clearly indicates the periodically arranged two-dimensional diffraction spots of the (1), (02) and (11) planes of Si with a face-centered cubic structure. Further, the lattice spacing is about 0.313 nm (as seen in Fig. 4(g)), corresponding to the (111) plane of Si. Therefore, a conclusion can be drawn that granular nanoparticles precipitated at cell boundaries are Si phases.

The performances of parts manufactured by laser rapid prototyping are depended on solidification structure. Furthermore, the solidification structure is determined by local solidification conditions (such as solidification rate R and temperature gradient G of the solid-liquid interface in molten pool). The influences of LEDs on microstructures perpendicular to building directions of SLM-processed AlSi10Mg parts are given in Fig. 5. Less Si phases precipitate at cell boundaries when the laser energy density is relatively low (as shown in Fig. 5(a)). This is because a lower energy density means a higher scan speed (since all other parameters are kept constant). A higher scan speed means that the cooling rate is higher since each spot is being subjected to the heat source for a shorter duration, so it solidifies faster. Consequently, the eutectic Si phase has insufficient time to precipitate from the Al matrix.

When the laser energy density is 131 J/mm^3, one can see dense and uniform cells and increasing Si phases at the cell boundaries (as shown in Fig. 5(b)). By comparison, the cell sizes and the number of the Si phases at the cell boundaries increased significantly when the laser energy density is 200 J/mm^3.This is because temperature gradient and cooling rate decrease caused by increasing of the laser energy density, and then resulting in most Si atoms are precipitated from the Al matrix. This brittle Si phase distributes at cell boundaries and it is detrimental to mechanical properties of the AlSi10Mg parts fabricated by P-SLM. In addition, more porosity can be observed (as shown in Fig. 5(c)). This is because burning losses of low melting Si and Mg elements caused by excessively high laser energy density. It has been reported in the literature [19] that both Si and Mg are lost during the SLM process for AlSi10Mg material.

The XRD patterns of raw AlSi10Mg powder and the P-SLM produced AlSi10Mg samples at different laser energy densities show the diffraction peaks of Al phase with face-centered cubic structure and Si phase with diamond cubic structure (as seen in Fig. 5(d)), and no obvious change of phase composition of the AlSi10Mg parts. However, intensities of the Al (111) and (002) peaks are reversed with respect to the raw powder. Moreover, the intensities of the Al (002) increase gradually while the intensities of other lattice planes decrease obviously with increasing LEDs. Peak elongation in XRD means that the material has undergone coarsening (as mentioned above) [20]. In addition, the intensity of the Si peaks is rather weak, which suggests that a reduced amount of “free” Si is present in the material. This can be attributed primarily to the extended solid solubility of Si in the α-Al: cellular morphology resulting from the high cooling rates observed during the P-SLM process.

Diagram of microstructure evolutions perpendicular to building directions for the AlSi10Mg parts fabricated by P-SLM is shown in Fig. 6. The alpha-Al precipitates from the liquid melt during the rapid solidification process of P-SLM. At about 800 K a eutectic reaction, corresponding to $L \rightarrow$α-Al + Si (eutectic) occurs. With the further decrease of the temperature, nano-sized secondary Si phases precipitate from the supersaturated α-Al and disperse uniformly in the matrix of the α-Al until complete solidification. Consequently, the microstructures are composed of α-Al + Si (eutectic) + Si (secondary) after complete recrystallization.

3.2. Mechanical properties

Microhardness values of the specimen perpendicular to the building directions at different LEDs are shown in Fig. 7**(a)**. There is little microhardness fluctuates between X, Y and 45° direction, and the microhardness values fluctuate between $HV_{0.1}110 \sim HV_{0.1}130$, which indicates that uniform distributions of microstructure and cell size in the

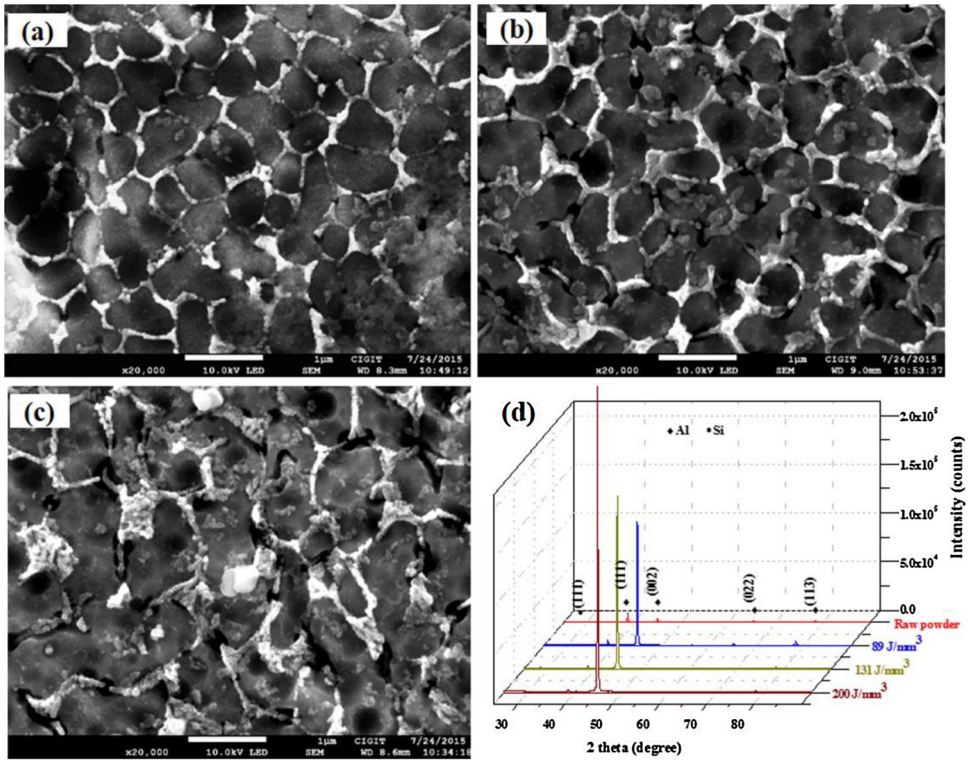

Fig. 5. Analysis of the microstructures perpendicular to building directions at different LEDs: (a) 89 J/mm^3; (b) 131 J/mm^3 (c) 200 J/mm^3 and (d) XRD patterns of the raw AlSi10Mg powder and the P-SLM-produced AlSi10Mg samples at different LEDs.

same processing plane. Meanwhile, the microhardness value of the P-SLM processed part is larger than that ($HV_{0.1}$ 95 ~ $HV_{0.1}$ 105) of the casting materials of the AlSi10Mg alloy [21]. This is due to formation of many fine cells caused by rapid heating and solidification in the process of P-SLM, and grain refinement strengthening improves the microhardness of the P-SLM processed AlSi10Mg part. Moreover, the uniform distribution of Si phase in the Al matrix and cell boundary is also beneficial to the increase of the microhardness of the P-SLM processed AlSi10Mg aluminum alloy part. In addition, the material hardness is shown to increase with LED until a maximum of 130 $HV_{0.1}$ at 131 J/mm^3. Further increases in LED display a reduction in material hardness. The hardness variations could also be attributed to the energy and subsequent temperature the laser has imparted to the material causing variations in heating/cooling rates. By optimizing the laser energy input, the hardness can be controlled. On the other hand, lower LED may cause the pores, semi-melted particles and other defects, while higher LED will lead to the balling effects. The production of the balling defects can lead to incontinuous powder layers and molten pools.

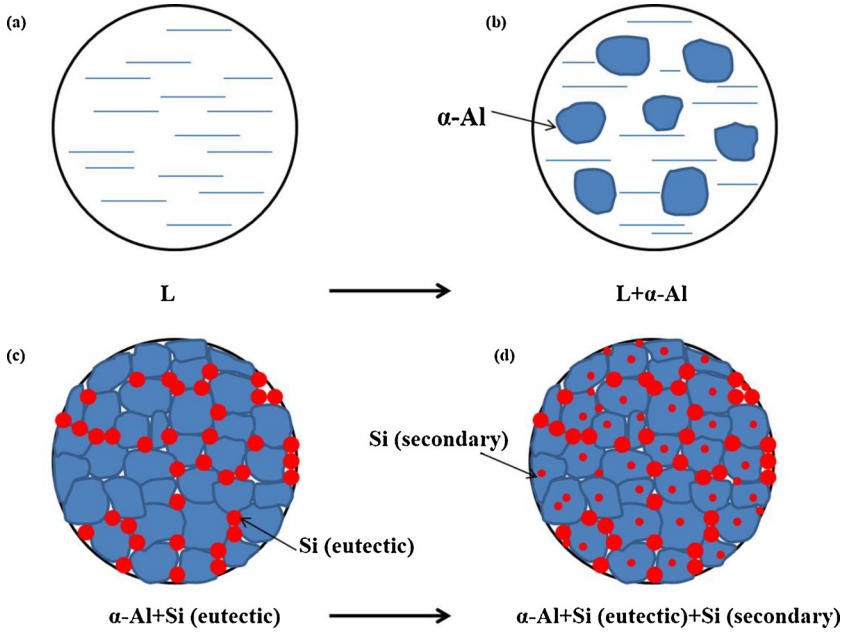

Fig. 6. Diagram of microstructure evolutions perpendicular to building directions for the P-SLM-fabricated AlSi10Mg parts: (a) stage of liquid melt; (b) stage of eutectic reaction; (c) end of solidification and (d) precipitation of secondary Si phases.

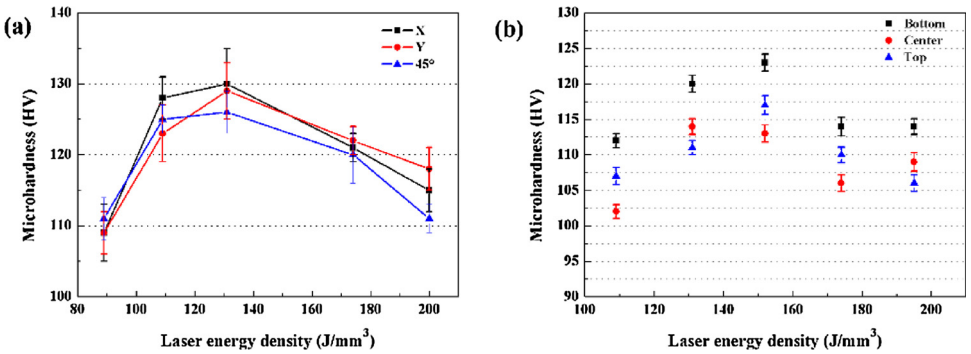

Fig. 7. Microhardness values of the specimens perpendicular to and along the building directions at different LEDs: (a) perpendicular to building directions and (b) along the building directions.

Consequently, the microhardness of the AlSi10Mg part decreased. Similar results were also reported by Aboulkhair et al. [22].

Microhardness of the specimens along the building directions at different LEDs are shown in Fig. 7**(b)**. The microhardness values fluctuate slightly and decrease with the increase of the building heights. This is mainly because the cooling rate and temperature gradient of the bottom layers are larger than those of the center and top layers, resulting in finer cells and larger residual stress, and then increase the microhardness. With the building height is getting higher, the temperature gradient is getting smaller caused by accumulation of heat. Therefore, the residual stress decreases. Meanwhile, the accumulated heat is equivalent to the heat treatment on the deposited layer, and it is also contributed to the release of residual stress. In this case, the microhardness of the P-SLMed part decreases gradually.

Mechanical properties of P-SLM built parts at different building directions and laser energy densities are shown in Table 2. When the laser energy density is 131 J/mm^3, the parts obtain the best comprehensive mechanical properties. The ultimate tensile strength (UTS) is 388 ± 10 MPa, yield strength (YS) is 257 ± 6 MPa, and elongation is 4.8 ± 0.50%. Moreover, mechanical properties of parts perpendicular to building directions are better than those of the samples along the building directions at the same laser energy density.

Comparisons for mechanical properties of P-SLM built AlSi10Mg parts and die-cast A360 parts are shown in Table 3. Compared with the mechanical properties of die-cast A360 parts, the SLMed samples display excellent mechanical properties, the UTS and YS of the AlSi10Mg samples fabricated by P-SLM are increased approximately 23.2% and 55.8%, respectively. In addition, the elongation is basically equal. This is because defects (such as segregation, porosity, impurities, coarse cells, and so on) are easy to form in cast AlSi10Mg samples, and then seriously affect the microstructures and mechanical properties. In comparison, during P-SLM process, the previous deposited powder layer can be partly remolten and realized a metallurgical combination with the new deposited layer. This is conducive to uniformity of the defects distribution and reducing the negative influence of defects on the mechanical properties of parts fabricated by P-SLM. Therefore, the P-SLM process can solve defects of traditional casting and significantly improve the mechanical properties of aluminum alloy parts.

Fracture surfaces of the samples processed by P-SLM under different laser energy densities are shown in Fig. 8. The fracture surfaces are completely covered with fine dimples (size of approximately 1 μm), indicating excellent ability to absorb the energy of the fracture and obvious plastic fracture characteristics, these can account for excellent tensile strength of the AlSi10Mg manufactured by P-SLM. Moreover, some cleavage planes with river patterns are displayed in the fracture surfaces (as seen in Fig. 8(a) and (d)), indicating brittle fracture characteristics, these can account for the relatively poor elongation of the AlSi10Mg manufactured by P-SLM. In addition, some large porosities (size of approximately 2–4 μm) exist in the fracture surfaces when the laser energy density is relatively high (200 J/mm^3), as shown in Fig. 8(c) and (f)). This is because the greater the laser energy density, the greater the temperature gradient and the faster the solidification rate. Therefore, the gas carried in AlSi10Mg powders could not escape from molten pool in time, and then resulting in porosities internally. These porosities are supposed to be the origin of crack initiation, and then cause the complete fracture of the sample.

Table 3
Summary of mechanical properties of AlSi10Mg alloys reported in literature, including results for selective laser melting (AlSi10Mg) and die casting (A360).

Reference	Heat treatment	Orientation	R_m (MPa)	R_p (MPa)	e_f (%)
This work	300 °C for 2 h	XY	388	257	4.8
		Z	378	239	4.3
[23]	300 °C for	XY	330	243	6.2
	2 h ± shot-peened	Z	329	231	4.1
[14]	(-)	XY	339	252	1.3
		Z	319	232	1.1
[24]	520 °C for 1 h + 160 °C	(-)	330	(-)	1.4
	for 6 h	(-)	294	(-)	3.9
[25]	As cast	(-)	315	165	3.5
[26]	As cast	(-)	315	165	5.0
[27]	As cast	(-)	315	165	4.0

4. Discussion

The mechanical properties of Al-Si alloy are mainly depended on the sizes of Al crystal and Si phase. These factors are greatly depended on solidification rate. For the traditional casting process, microstructure is

Table 2
Mechanical properties of SLM built parts at different building directions and laser energy densities. R_m is ultimate tensile strength, R_p is yield strength, e_f is tensile elongation.

Laser energy density (J/mm^3)	Perpendicular to building directions (XY)			Along the building directions (Z)		
	R_m (MPa)	R_p (MPa)	e_f (%)	R_m (MPa)	R_p (MPa)	e_f (%)
89	370 ± 8	246 ± 5	4.4 ± 0.30	370 ± 8	237 ± 5	4.2 ± 0.30
131	388 ± 10	257 ± 6	4.8 ± 0.50	378 ± 6	239 ± 9	4.3 ± 0.25
200	355 ± 11	230 ± 6	4.0 ± 0.4	355 ± 7	220 ± 8	4.0 ± 0.20

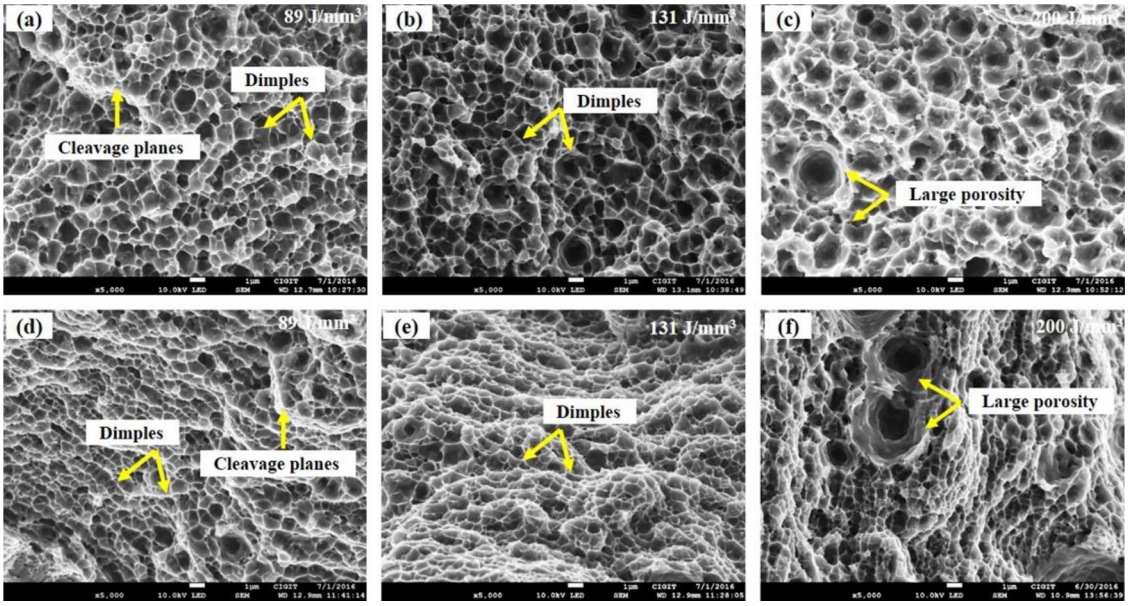

Fig. 8. Fracture surfaces of the P-SLM samples under different laser energy densities: (a)~(c) perpendicular to building directions; (d)~(f) along the building directions.

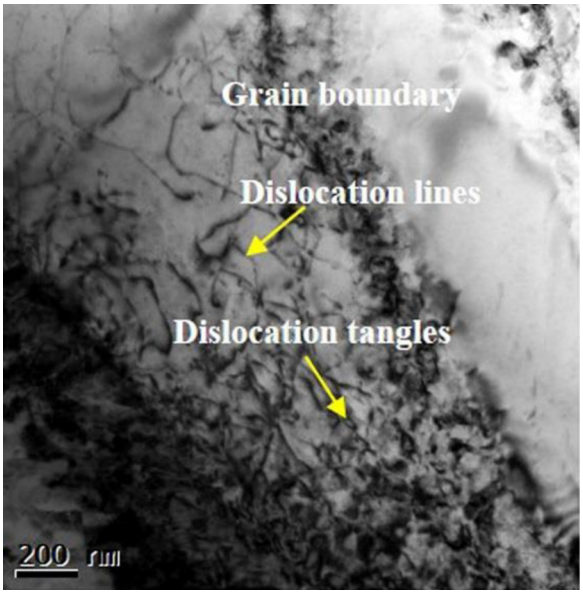

Fig. 9. Dislocation morphologies in microstructure of AlSi10Mg sample produced by P-SLM.

coarse and atom supersaturation is low caused by relatively low solidification rate. Consequently, the mechanical properties of Al-Si alloys are relatively poor. In contrast, it is prone to obtain extremely fine cells and high supersaturation because of rapid cooling in the P-SLM process, so that the P-SLM part has high mechanical properties. In this study, main strengthening mechanisms of mechanical properties of the AlSi10Mg produced by P-SLM may be summarized as follows:

(1) Solid solution strengthening: The interstitial Si atoms are dissolved in the crystal lattice of Al, resulting in lattice distortion of Al, local stress fields are formed that interact with those of the dislocations, impeding their motion and causing an increase in the yield stress of the material, which means an increase in strength of the material. According to the research results of Shercliff and Ashby, solid solution strengthening is described mathematically by equation:

$$\sigma ss = a\overline{C}^{2/3} \quad (5)$$

where σ_{ss} is solid solution strengthening effect, a is a materials constant, $\overline{C}$ is the average concentration of the solute atoms. Because velocity of melting and solidification during the SLM is very fast, The Si atom is in a state of supersaturation in the Al matrix, resulting in great value of the $\overline{C}$, and then it has stronger solid solution strengthening effect.

(2) Grain refinement strengthening: Theoretically, the smaller the grain size, the more the number of grains in a certain volume, indicating the strain differences between inside grains and grain boundaries are little under the action of the same external force. In this case, it is not easy to cause fracture caused by stress concentration. Therefore, the specimens can bear relatively large deformation before fracture, and then get excellent mechanical properties. The relation between yield stress and grain size is described mathematically by the Hall-Petch equation:

$$\sigma \text{ y} = \sigma 0 + kd^{-1/2} \quad (6)$$

where σy is the yield stress, $\sigma 0$ is a materials constant for the starting stress for dislocation movement (or the resistance of the lattice to dislocation motion), k is the strengthening coefficient, and d is the average grain diameter. In this study, the average grain size of the P-SLMed AlSi10Mg part is about 1 μm, it is much smaller than that of the traditional casting parts, and then it has significant effects on grain refinement strengthening.

(3) Dislocations strengthening: High density dislocation tangle and dislocation networks are found in the microstructures (as shown in Fig. 9). This is because P-SLM is a rapid heating and cooling process, and has the characteristics of cumulative processing on micro scale. Hence, many dislocation groups are produced caused by repeated and extremely fast heating and cooling. Meanwhile, there are strong interactions and synergism between dislocations. However, dislocation motions are limited due to the pinning effect of cell boundaries and uniform distributed second phase, resulting in dislocation pile up between the precipitates. In this case, the dislocation piles up cause lattice distortion, and then resulting in internal stress. The internal stress has an important influence on the mechanical properties of the P-SLMed parts. Wu et al. [28] studied strength of selectively laser melted AlSi10Mg, they observed that

cell boundaries, sub-cell boundaries and particles within the cells limit dislocation movement during deformation.

(4) Second-phase strengthening: The brittle second phase Si particles disperse uniformly in the Al matrix, which hinder the movement of the dislocations, and enhance the deformation resistance of the AlSi10Mg alloy, thus increasing the strength of the AlSi10Mg parts fabricated by P-SLM.

5. Conclusions

The effects of LEDs on microstructure evolutions and mechanical properties of AlSi10Mg powders fabricated by pulsed selective laser melting were investigated. The main conclusions are summarized as follows:

(1) The solidification microstructures show fine cellular structures and are composed of α-Al, eutectic Si, and secondary Si. Moreover, the amounts of the Si phases at the cell boundaries increase gradually with increasing of the LEDs, while excessive high energy input may result in porosity.

(2) The microhardness values of the specimens perpendicular to the building directions fluctuate between $HV_{0.1}$ 110 ~ $HV_{0.1}$ 130. In comparison, the microhardness values of the specimens along the building directions decrease with the increase of the building heights. Furthermore, the P-SLMed samples display much more excellent mechanical properties than those of the casting AlSi10Mg, and the fracture surfaces illustrate mixed characteristics of plastic fracture and brittle fracture.

(3) The strengthening mechanisms of mechanical properties of the AlSi10Mg produced by P-SLMed mainly include solid solution strengthening, grain refinement strengthening, dislocations strengthening and second-phase strengthening.

Acknowledgements

The study is supported by the National Natural Science Foundation of China (NSFC, China) under Grant Number of 51405467, and Chongqing Research of Application Foundation and Advanced Technology (project No. cstc2016jcyj A0061).

References

[1] Li W, Li S, Liu J, Zhang A, Zhou Y, Wei Q, et al. Y: Mater. Sci. Eng. A 2016;663:116–25.
[2] Tradowsky U, White J, Ward RM, Read N, Reimers W, Attallah MM. Mater Des 2016;105:212–22.
[3] Wang LZ, Liu Y, Chang S. Metall. Mater. Trans. A 2016;47:2444–53.
[4] Caceres CH, Davidson CJ, Griffiths JR. Mater. Sci. Eng. A 1995;197:171–9.
[5] Herzog D, Seyda V, Wycisk E, Emmelmann C. Acta Mater 2016;117:371–92.
[6] Gu DD, Meiners W, Wissenbach K, Poprawe R. Int. Mater. Rev 2012;57:133–64.
[7] Zhang BC, Liao HL, Coddet C. Mater Des 2012;34:753–8.
[8] Olakanmi EO, Cochrane RF, Dalgarno KW. Prog Mater Sci 2015;74:401–77.
[9] Gu DD, Wang HQ, Zhang GQ. Metall. Mater. Trans. A 2014;45:464–76.
[10] Das M, Balla VK, Basu D, Bose S, Bandyopadhyay A. Scripta. Mater 2010;63:438–41.
[11] Kempen K, Thijs L, Van Humbeeck J, Kruth JP. Phys Procedia 2012;39:439–46.
[12] Brandl E, Heckenberger U, Holzinger V, Buchbinder D. Mater Des 2012;34:159–69.
[13] Thijs L, Kempen K, Kruth JP, Humbeeck JV. Acta Mater 2013;61:1809–19.
[14] Read N, Wang W, Essa K, Attallah MM. Mater Des 2015;65:417–24.
[15] Wang LZ, Wang S, Wu JJ. Opt Laser Technol 2017;96:88–96.
[16] Thijs L, Verhaeghe F, Craeghs T, Humbeeck JV, Kruth JP. Acta Mater 2010;58:3303–12.
[17] Tang M, Pistorius PC. Int J Fatigue 2016;94:192–201.
[18] Kim DK, Woo W, Hwang JH. J Alloys Compd 2016;686:281–6.
[19] Aboulkhair NT, Everitt NM, Ashcroft I, Tuck C. Addit Manuf 2014;1-4:77–86.
[20] Prashanth KG, Scudino S, Klauss HJ, Surreddi KB, Löber L, Wang Z, et al. Mater Sci Eng A 2014;590:153–60.
[21] Zhang Y, Gao T, Liu X. J Alloys Compd 2014;585:442–7.
[22] Aboulkhair NT, Maskery I, Tuck C, Ashcroft I, Everitt NM. J Mater Process Technol 2016;230:88–98.
[23] Manfredi D, Calignano F, Krishnan M, Canali R, Ambrosio E, Atzeni E. Materials 2013;6:856–69.
[24] Maskery I, Aboulkhair NT, Tuck C, Wildman RD, Ashcroft IA, Everitt NM. Solid Freeform Fabrication Symposium. 2015. p. 1017–25.
[25] ASTM B85. Standard specification for aluminum-alloy die castings. West Conshohocken (PA): ASTM International; 2013.
[26] Kearney AL. Properties of cast aluminum alloys. In: ASM International Handbook Committeeeditor. ASM handbook volume 2: properties and selection: nonferrous alloys and special-purpose materials. Materials Park (Ohio): ASM International; 1990. p. 152–77.
[27] Kaufman JG. Properties of Aluminum Alloys: Fatigue Data And The Effects Of Temperature, Product Form, and Processing. Materials Park (Ohio): ASM International; 2008. p.15.
[28] Wu J, Wang XQ, Wang W, Attallah MM, Loretto MH. Acta Mater 2016;117:311–20.